THE ASTROPHYSICAL JOURNAL, 414:815–829, 1993 September 10

A SEMIANALYTIC MODEL FOR CYCLOTRON LINE FORMATION

J. C. L. WANG,[1] I. WASSERMAN,[2] AND D. Q. LAMB[3]
Received 1992 December 9; accepted 1993 March 19

ABSTRACT

We present here a *semi-analytic, physically motivated* model for the formation of the cyclotron *first harmonic* line, as well as higher harmonic lines. The model is based upon three basic physical principles: (1) the radiative transfer is a smooth stochastic process, (2) the first harmonic feature forms from complete redistribution in a single *block* of resonant photon scatters, and (3) the higher harmonics are well-approximated as "true" absorption features. The emergent spectral shapes are expressed as quadratures. This model includes the essential relativistic effects and is valid for weak fields ($B \ll B_c = 4.414 \times 10^{13}$ G) in static media where the first harmonic is optically thick in the line core but not in its wings. This is a regime that may be relevant for the many classical γ-ray burst sources where low-energy absorption-like features have been observed. To illustrate this model, we consider the line transfer using polarization-averaged scattering profiles derived using nonrelativistic quantum mechanics but with relativistic kinematics. This model approximates well the corresponding exact physical model as calculated using Monte Carlo methods, and is at least an order of magnitude faster to compute than the Monte Carlo simulations. As such, it can be used as a practical substitute for the more time consuming simulations to perform complete analysis of cyclotron lines in potentially large numbers of classical γ-ray burst sources. Since the semi-analytic model is based upon only a few simple physical principles, it should be easily adaptable to more general physical situations, such as to line formation in dynamic media. Owing to its relative simplicity and speed, such a semi-analytic model offers the promise of liberating the researcher from large codes and time consuming simulations in the analysis of cyclotron line spectra.

Subject headings: gamma rays: bursts — line: formation — radiative transfer

1. INTRODUCTION

Cyclotron lines are a powerful diagnostic tool in high energy astrophysics. The discovery of cyclotron features in the spectra of several binary X-ray pulsars (Trümper et al. 1979; Wheaton et al. 1981; Clark et al. 1990) provided direct confirmation of the existence of superstrong magnetic fields, thereby supporting the association of X-ray pulsars with strongly magnetized accreting neutron stars. Absorption-like features at $\approx$30–80 keV have been reported in $\sim$15% of "classical" γ-ray bursts (Mazets et al. 1981; Hueter 1983). These were interpreted as cyclotron line features (Mazets et al. 1980, 1981) and were among the first pieces of evidence suggesting magnetized neutron stars as possible sources of classical γ-ray bursts. Although many of these observations remain controversial, the observations of harmonically separated absorption-like features of high statistical significance between 20 and 50 keV in three classical γ-ray bursts by the *Ginga* satellite (Murakami et al. 1988; Yoshida et al. 1991) lends support to the cyclotron interpretation of these features (Fenimore et al. 1988; Harding & Preece 1989; Lamb et al. 1989; Alexander & Mészáros 1989; Wang et al. 1989b). The *Ginga* observations suggest that at least some of the classical γ-ray bursts originate from strongly magnetized neutron stars.

In order to fully exploit the diagnostic power of the cyclotron lines, it is necessary to accurately model the line formation and to do detailed statistical comparisons between data and theoretical spectra. Thus, for instance, such theoretical modeling and comparisons with data led to a *quantitative* explanation of the positions, shapes, and equivalent widths of the observed low-energy features in a spectrum of the classical γ-ray burst GB 880205 (Lamb et al. 1989; Alexander & Mészáros 1989; Wang et al. 1989b). This success of the cyclotron line formation model strongly suggested that the burst GB 880205 originated from a magnetized Galactic neutron star.

In the cyclotron line formation model, the first harmonic is formed from multiple resonant scatters, and its shape must be determined, in general, from a numerical radiative transfer calculation that also accounts for the important higher harmonics. This is because in weak fields ($B \ll B_c$), higher harmonic photons may undergo resonant Raman scattering, thereby "spawning" additional photons at the first harmonic. Since the higher harmonics are formed from Raman scattering, their shapes are well approximated as absorption lines.

The line formation modeling carried out to date, both on accreting magnetized neutron star sources and on γ-ray bursters, rely on radiative transfer calculations using either finite differencing methods, such as the Feautrier technique (Mihalas 1978; Nagel 1980; Mészáros & Nagel 1985; Alexander & Mészáros 1989), or Monte Carlo methods (Avery & House 1968; Wang, Wasserman, & Salpeter 1988, 1989a; Lamb et al. 1989; Wang et al. 1989b). While physically accurate, these calculations demand considerable CPU

[1] Canadian Institute for Theoretical Astrophysics, University of Toronto, 60 St. George Street, Toronto, ON, Canada M5S 1A7.
[2] Center for Radiophysics and Space Research, Cornell University, Ithaca, NY 14853.
[3] Department of Astronomy and Astrophysics, University of Chicago, 5640 South Ellis Avenue, Chicago, IL 60637.

expenditure, with the bulk of the computational effort going toward simulating the formation of the first harmonic. As a result, it becomes a very slow, even impractical, task to perform complete analysis of cyclotron lines on even a small sample of sources. The analysis of GB 880205 by Wang et al. (1989b), for example, required one full month of CPU time on an FPS-164.

An alternative approach to numerical modeling is to fit purely phenomenological models—such as the traditional Gaussian line shape—to the observed lines. This procedure is fast, but is not physically motivated. While such an approach yields a mathematical description of the lines, it only offers semiquantitative insight into the physics of line formation.

We present here a *semi-analytic, physically motivated* model of cylotron line formation. This model is valid in weak fields ($B \ll B_c$) and moderately thick media where the cyclotron first harmonic is optically thick in the line core but optically thin in the wings. In this regime, the resonant transfer of first harmonic photons may be viewed approximately as first harmonic photons in the line core suffering a "block" of (core) scatters before escaping the medium in the line wings in one scatter-free excursion. The central assumptions underlying this model are (1) the radiative transfer is a smooth stochastic process, (2) the first harmonic feature forms from complete redistribution in a single *block* of resonant photon scatters (Wasserman & Salpeter 1980), and (3) the higher harmonics are well-approximated as "true" absorption features. In this model, the computation of the emergent line shapes is reduced to quadratures. The regime in which this model is valid may apply in the classical γ-ray burst sources that show absorption-like features in their low-energy spectra, but is probably not applicable to the line-forming regions in magnetized accreting neutron stars where the first harmonic is believed to be very optically thick in the wings (see, e.g., Mészáros & Nagel 1985; Wang et al. 1989a). In addition to being a reasonable physical approximation to the exact model, the *s*emi-*a*nalytic *m*odel discussed here (hereafter referred to as SAM) is at least an order of magnitude faster to compute than the (exact) Monte Carlo simulations. As such, it becomes a feasible tool for analyzing low-energy line features in potentially large numbers of classical γ-ray burst spectra. These spectra may become available when the burst data from the *Ginga* satellite are fully reduced and when more bright bursts are observed by the BATSE experiment onboard the *Compton Gamma-Ray Observatory* (*CGRO*).

Since the SAM is based upon only a few general physical principles, it should be fairly easy to extend to more complex physical situations (e.g., line formation in dynamic media, non–plane-parallel geometry). Combined with its speed, models of this genre may therefore become a practical alternative to large time consuming simulations in the analysis of cyclotron line spectra.

In § 2, we describe the physical ideas behind SAM. We then derive the SAM expression for the first harmonic line shape ignoring the effect of spawning from higher harmonics. We also derive in this section the expression for the higher harmonic line shapes. In § 3, we derive the SAM expression for the first harmonic line shape taking into account spawning from the second harmonic. We discuss our results and give the conclusions in § 4. The SAM formalism presented here apply in general to polarized resonant line transfer. For the purposes of illustrating the salient features of the model, however, we shall specialize in our examples to unpolarized line transfer where we use polarization-averaged scattering profiles derived using nonrelativistic quantum mechanics but with relativistic kinematics. To realistically model the emergent line spectra, one should in general use polarized line transfer, especially for the formation of the higher cyclotron harmonics (Alexander & Mészáros 1989).

2. THE FIRST AND HIGHER HARMONICS: NO SPAWNING

For specificity, we consider a plane-parallel slab with column depth N_e (in electrons cm^{-2}) for the line-forming region. We assume that a uniform magnetic field of strength B threads the slab oriented parallel to the slab normal. We assume the region to be populated by electrons with a (quasi-)thermal distribution of momenta parallel to the field at a constant temperature T. This is a reasonable assumption since Monte Carlo simulations suggest that the temperature of the line-forming region does not depend sensitively upon the column depth of the slab (Lamb, Wang, & Wasserman 1990, hereafter LWW). The motion of electrons orthogonal to the field is quantized into Landau levels. We assume that all electrons reside in the ground state Landau level. We consider purely scattering slabs where the dominant radiative process is cyclotron resonant scattering. These conditions apply in superstrong field environments ($B \sim 10^{12}$ G) for slabs of low density and moderate thickness. We assume here that the resonant scattering layer is static, deferring to a future paper the extension to dynamic media.

To set the scales involved in this work, the polarization-, angle-, and frequency-averaged optical depth in the first harmonic is given by

$$\tau_1 = 100 N_{e,21} B_{12}^{-1} \left(\frac{T}{\text{keV}}\right)^{-1/2}, \tag{1}$$

where $B = 10^{12} B_{12}$ G, $N_e = 10^{21} N_{e,21}$ electrons cm^{-2}, and T is in keV. For slabs that are optically thick in the core of the first harmonic but optically thin in its wings,

$$1 \ll \tau_1 \lesssim 1/a, \tag{2}$$

where $a = \Gamma_{\text{rad}}/2\omega_D = 1.8 \times 10^{-3} B_{12} (T/\text{keV})^{-1/2}$ is the dimensionless natural line width (Wasserman & Salpeter 1980; Wang et al. 1988), $\Gamma_{\text{rad}} = 2.6 \times 10^{-3} B_{12}^2 (\text{keV})$ is the radiative width, $\omega_D = \omega_B (2T/m_e)^{1/2}$ is the Doppler width, and $\omega_B = 11.6 B_{12} (\text{keV})$ is the classical energy of the cyclotron first harmonic. (Without exception, we adopt units in which $\hbar = c = k_B = 1$, with k_B the Boltzmann constant.) Equation (2) is equivalent to

$$0.01 B_{12} \left(\frac{T}{\text{keV}}\right)^{1/2} \ll N_{e,21} \lesssim 6 \left(\frac{T}{\text{keV}}\right). \tag{3}$$

The corresponding optical depths in the second and third cyclotron harmonics are

$$\tau_2 = 1.4 N_{e,21}\left(\frac{T}{\mathrm{keV}}\right)^{-1/2}, \tag{4}$$

$$\tau_3 = 0.08 N_{e,21} B_{12}\left(\frac{T}{\mathrm{keV}}\right)^{-1/2}. \tag{5}$$

[The polarization-, angle-, and frequency-averaged optical depth is defined here as $\tau_n = \int_0^\infty d\omega/\omega_{\mathrm{D},n} \int d\Omega/4\pi \tau_n(\omega, \mu)$, where $\tau_n(\omega, \mu)$ is the polarization-averaged optical depth for the nth harmonic (cf. Appendix). These values correspond to $1/n$ times those in LWW (cf. their eqs. [1], [3], and [4]) who used $\omega_{\mathrm{D},1}$ in place of $\omega_{\mathrm{D},n}$ in their definition of τ_n. The definition used here is a more "natural" one.] The polarization-averaged line-center optical depths at the first three harmonics, $\tau_n^0 \equiv \tau_n(\omega = \omega_n, \mu)$ (cf. Appendix; eq. [A1]), are given by

$$\begin{aligned}
\tau_1^0 &= 43 B_{12}^{-1}\left(\frac{T}{\mathrm{keV}}\right)^{-1/2} \frac{[N_{e,21}(1+\mu^2)]}{|\mu|}, \\
\tau_2^0 &= 0.97\left(\frac{T}{\mathrm{keV}}\right)^{-1/2} \frac{[N_{e,21}(1+\mu^2)\sin^2\theta]}{|\mu|}, \\
\tau_3^0 &= 0.072 B_{12}\left(\frac{T}{\mathrm{keV}}\right)^{-1/2} \frac{[N_{e,21}(1+\mu^2)\sin^4\theta]}{|\mu|},
\end{aligned} \tag{6}$$

where $\theta = \cos^{-1}\mu$ is the photon propagation angle relative to the field. (Equations [1], [4], [5], and [6] are used to set the scales involved in this work. In obtaining these equations [and *only* for these equations], we have, for simplicity, used the weak field resonant cross sections with zero natural line width and nonrelativistic kinematics.)

In contrast, the continuum optical depth is

$$\tau_c \approx \sigma_{\mathrm{T}} N_e = 6.7 \times 10^{-4} N_{e,21}, \tag{7}$$

where $\sigma_T = 6.65 \times 10^{-25}$ cm^2 is the Thomson cross section. In moderately thick media (see eqs. [2]–[3]), we may therefore ignore continuum scattering as regards *line formation* (see LWW).

Photons in the core of the first harmonic [$\Delta E_{\mathrm{core}} \sim \omega_{\mathrm{D}}(\ln \tau_1)^{1/2}$] travel a short distance (core mean free path $\ll$ slab width) before being scattered. After suffering many resonant scatters, they escape into the wings in a rare core-wing transition (cf. Wasserman & Salpeter 1980). During their stay in the core, the photons do not travel a large distance because their mean free paths are short, and they do not redistribute significantly in frequency ($\Delta\omega \lesssim \omega_{\mathrm{D}}$). In moderately thick media, photons escape the slab with essentially no further scattering once they enter the wings. The escape frequency and angle is then simply the emergent frequency and angle of the core-wing transition resonant scattering event. The resonant transfer of first harmonic photons may therefore be viewed approximately as first harmonic core photons suffering a block of (core) scatters before escaping the medium in one scatter-free excursion.

Let $\boldsymbol{k}'$ denote all properties of the photon (frequency, direction, polarization) just before it enters a block of scatters, and let $\boldsymbol{k}$ denote these properties just after it exits the scattering block. Let the thermally averaged resonant scattering cross section (that is, the resonant scattering profile) for first harmonic photons be defined as

$$\sigma_1(\boldsymbol{k})/\sigma_{\mathrm{T}} = \phi_1(\boldsymbol{k}). \tag{8}$$

Let $r(\boldsymbol{k}' \to \boldsymbol{k}, \boldsymbol{x})$ denote the "block redistribution function," that is, the probability that a photon with parameters $\boldsymbol{k}$ emerge from a *block* of scatters given that the photon entered the block located at position $\boldsymbol{x}$ with parameters $\boldsymbol{k}'$. In an isothermal medium, $r(\boldsymbol{k}' \to \boldsymbol{k}, \boldsymbol{x}) = r(\boldsymbol{k}' \to \boldsymbol{k})$. In addition, for a sufficiently large number of scatters (N) in the block (Wasserman & Salpeter 1980),

$$\lim_{N\to\infty} r(\boldsymbol{k}' \to \boldsymbol{k}) = \phi_1(\boldsymbol{k}). \tag{9}$$

This corresponds to complete redistribution from a *block* of scatters as opposed to a single scatter and is therefore termed "generalized complete redistribution" (Wasserman & Salpeter 1980).

Consider a slab with photons injected from "below" and with the observer on the "top" side. We take the magnetic field $\boldsymbol{B}$ to be parallel to the slab normal. Define $\tau = 0$ at the top and $\tau = \tau_0 = \sigma_T N_e$ at the bottom. With μ the direction cosine of photons measured with respect to $\boldsymbol{B}$, we call photons escaping from the top of the slab with $\mu > 0$ "transmitted" photons, and those escaping from the bottom with $\mu < 0$ "reflected" photons. Quite generally, given an incident photon intensity $N_i(\boldsymbol{k})[\propto \Theta(\mu)$ for upwardly isotropic injection; in photons cm^{-2} s^{-1} keV^{-1} sr^{-1}], we write the transmitted ($\mu > 0$) photon intensity as

$$N_T(\boldsymbol{k}) = N_i(\boldsymbol{k}) \exp\left[\frac{-\tau_0\,\phi(\boldsymbol{k})}{\mu}\right] + \int_0^{\tau_0} d\tau \int_{\mu'>0} d\boldsymbol{k}'\, q_T(\boldsymbol{k}' \to \boldsymbol{k}, \tau)\phi_1(\boldsymbol{k}') \frac{\exp\left[-(\tau_0 - \tau)\phi_1(\boldsymbol{k}')/\mu'\right]}{\mu'} N_i(\boldsymbol{k}'), \tag{10}$$

where $\phi(\boldsymbol{k}) = \Sigma_n \phi_n(\boldsymbol{k})$. In equation (10), $q_T(\boldsymbol{k}' \to \boldsymbol{k}, \tau)$ gives the distribution of transmitted photon properties given that the first scatter occurred at depth τ with incident photon properties $\boldsymbol{k}'$. As such, it contains all the microphysics of the scattering resonant transfer. The first term gives the "absorption" contribution to the transmitted intensity, or more precisely, the contribution from photons that did not scatter out of the line-of-sight. The function $\phi(\boldsymbol{k})$ in this term is the total scattering profile which includes all the relevant higher harmonics. Since the second and higher harmonics are effectively true absorption lines owing to photon spawning

from resonant Raman scattering (Bussard & Lamb 1982; Fenimore et al. 1988; Lamb et al. 1989; Wang et al. 1989b), this term is an excellent approximation to the shape of these higher harmonics. The second term gives the contribution to the shape of the first harmonic from multiple resonant scatters. Spawning from the second and higher harmonics can be included by altering $N_i(\boldsymbol{k}')$ in the integrand (see § 3). For the discussion in this section, spawning is not included. The neglect of spawning is a valid approximation when $\tau_2 \ll 1$, that is, when $N_{e,21} \ll 0.7(T/\mathrm{keV})^{1/2}$ (cf. eq. [4]; § 3).

Analogously, the reflected photon intensity is given by

$$N_R(\boldsymbol{k}) = \int_0^{\tau_0} d\tau \int_{\mu'>0} d\boldsymbol{k}' q_R(\boldsymbol{k}' \to \boldsymbol{k}, \tau)\phi_1(\boldsymbol{k}') \frac{\exp\left[-(\tau_0 - \tau)\phi_1(\boldsymbol{k}')/\mu'\right]}{\mu'} N_i(\boldsymbol{k}') , \tag{11}$$

where $q_R(\boldsymbol{k}' \to \boldsymbol{k}, \tau)$ plays the same role as $q_T(\boldsymbol{k}' \to \boldsymbol{k}, \tau)$ but for reflected photons. Since first harmonic photons are neither destroyed nor created by resonant scattering, they eventually escape the slab. Consequently,

$$\int d\boldsymbol{k}[q_T(\boldsymbol{k}' \to \boldsymbol{k}, \tau) + q_R(\boldsymbol{k}' \to \boldsymbol{k}, \tau)] = 1 . \tag{12}$$

Setting $\phi(\boldsymbol{k}) = \phi_1(\boldsymbol{k})$ in eq. (10), integrating the sum of equations (10) and (11) over $\boldsymbol{k}$, and using equation (12) gives

$$\int d\boldsymbol{k}[N_T(\boldsymbol{k}) + N_R(\boldsymbol{k})] = \int d\boldsymbol{k} N_i(\boldsymbol{k}) , \tag{13}$$

which expresses photon number conservation of first harmonic photons, as required.

Adopting the picture of escape after a single block of scatters, we interpret $q_T(\boldsymbol{k} \to \boldsymbol{k}, \tau)[q_R(\boldsymbol{k}' \to \boldsymbol{k}, \tau)]$ as the probability that photons are transmitted (reflected) with properties $\boldsymbol{k}$ given that the single block of scatters occurred at depth τ with incident photon properties $\boldsymbol{k}'$. Using generalized complete redistribution upon the block of scatters (eq. [9]), we obtain

$$q_T(\boldsymbol{k}' \to \boldsymbol{k}, \tau) = \frac{\phi_1(\boldsymbol{k}) \exp\left[-\tau\phi_1(\boldsymbol{k})/\mu\right]}{Q(\tau)} ; \qquad \mu > 0 ; \tag{14}$$

$$q_R(\boldsymbol{k}' \to \boldsymbol{k}, \tau) = \frac{\phi_1(\boldsymbol{k}) \exp\left[-(\tau - \tau_0)\phi_1(\boldsymbol{k})/\mu\right]}{Q(\tau)} ; \qquad \mu < 0 ; \tag{15}$$

where

$$Q(\tau) = \int d\boldsymbol{k}\phi_1(\boldsymbol{k})\{\exp\left[-\tau\phi_1(\boldsymbol{k})/\mu\right]\Theta(\mu) + \exp\left[-(\tau - \tau_0)\phi_1(\boldsymbol{k})/\mu\right]\Theta(-\mu)\} \tag{16}$$

from equation (12), and where $\Theta(\mu)$ is the Heaviside step function [$\Theta(x) = 1$ for $x \geq 0$ and is zero otherwise]. The most probable escape frequency for transmission is given by the roots of $dq_T(\boldsymbol{k}' \to \boldsymbol{k}, \tau)/d\omega = 0$, that is, by $[1 - \tau\phi_1(\boldsymbol{k})/\mu]d\phi_1(\boldsymbol{k})/d\omega = 0 (\mu > 0)$. (The discussion for the most probable escape frequency for reflection is identical but with $q_T \to q_R$.) In an optically thin medium, $\tau\phi_1(\boldsymbol{k})/\mu < 1$, and the most probable escape frequency is simply the frequency corresponding to the peak value of $\phi_1(\boldsymbol{k})$. In an optically thick medium, the most probable escape frequency is given by $\tau\phi_1(\boldsymbol{k}) = \mu$, which is simply the frequency at which a photon with properties $\boldsymbol{k}$ see unit optical depth along a line-of-sight through the slab. This characteristic of the most probable escape frequency is valid if the media is optically thick in the line core but not in its wings, that is, if equation (2) is valid. For illustration, adopt the nonrelativistic polarization-averaged scattering profile with zero natural line width, that is,

$$\phi_1(\boldsymbol{k}) = s_0 \frac{3/4(1 + \mu^2)}{|\mu|} \frac{e^{-(x/\mu)^2}}{\sqrt{\pi}} \tag{17}$$

(cf. Wasserman & Salpeter 1980), where $x \equiv (\omega - \omega_B)/\omega_D$ and $s_0 = (\pi m_e)/(2e^2\omega_D)$ (e^2 is the Sommerfeld fine structure constant). Taking $\mu = 0.5$ to be a representative direction cosine and using $\tau\phi_1(\boldsymbol{k})/\mu = 1$, we obtain the well-known result for the mean escape frequency $[x/\mu]_{esc}$ when $1 \ll \tau_1 \ll 1/a$ (see, e.g., LWW),

$$\left(\frac{x}{\mu}\right)_{esc} \approx \left[\ln\left(\frac{15}{4}\frac{s_0\tau}{\sqrt{\pi}}\right)\right]^{1/2} \sim [\ln\tau_1]^{1/2} , \tag{18}$$

where $\tau_1 = s_0\tau$ is the polarization-angle-frequency averaged first harmonic optical depth corresponding to a Thomson depth of τ (see eq. [1]).

We specialize now to unpolarized transfer. To this end, we use in equations (8)–(16) the polarization-averaged scattering profiles with zero natural line width but incorporating relativistic kinematics (cf. Appendix). For the cyclotron first harmonic which is formed from multiple resonant scatters, unpolarized transfer is a valid approximation for low electron densities ($n_e \ll 10^{22}B_{12}^4$ cm^{-3}), where strong field vacuum polarization determines the photon propagation modes (cf. Gnedin, Pavlov, & Shibanov 1978; Mészáros & Ventura 1978). For the higher harmonics which are determined by at most a few scatters, the order unity difference between the cross sections of the two photon polarization modes may be important (Alexander & Mészáros 1989). The zero line width approximation is valid when the media is optically thin in the wings of the first harmonic. The relativistic kinematics is crucial in giving the asymmetric line shapes that are especially evident at photon propagation angles nearly orthogonal to the field (Lamb

et al. 1989). We emphasize that the use of polarization-averaged cross sections is *not* a restriction of SAM; the SAM formalism discussed above (see eqs. [8]–[16]) apply in general to polarized resonant line transfer.

From equations (10), (11), (14), and (15), the unpolarized transmitted (N_T; $\mu > 0$) and reflected (N_R; $\mu < 0$) spectra are given by

$$N_T(\omega, \mu) = N_i(\omega, \mu) \exp\left[\frac{-\tau_0 \phi(\omega, \mu)}{\mu}\right] + \int_0^{\tau_0} d\tau \int_0^1 d\mu' \int_0^\infty d\omega' \frac{\exp\left[-\tau\phi_1(\omega, \mu)/\mu\right]}{Q(\tau)} \phi_1(\omega, \mu)\phi_1(\omega', \mu') \frac{\exp\left[-(\tau_0 - \tau)\phi_1(\omega', \mu')/\mu'\right]}{\mu'} N_i(\omega', \mu') ; \quad (19)$$

$$N_R(\omega, \mu) = \int_0^{\tau_0} d\tau \int_0^1 d\mu' \int_0^\infty d\omega' \frac{\exp\left[-(\tau - \tau_0)\phi_1(\omega, \mu)/\mu\right]}{Q(\tau)} \phi_1(\omega, \mu)\phi_1(\omega', \mu') \frac{\exp\left[-(\tau_0 - \tau)\phi_1(\omega', \mu')/\mu'\right]}{\mu'} N_i(\omega', \mu') . \quad (20)$$

From equation (16) and the identity $\phi_n(\omega, \mu) = \phi_n(\omega, -\mu)$ (cf. Appendix), the normalization $Q(\tau)$ is given by

$$Q(\tau) = \int_0^\infty d\omega \int_0^1 d\mu\, \phi_1(\omega, \mu)\{\exp\left[-\tau\phi_1(\omega, \mu)/\mu\right] + \exp\left[-(\tau_0 - \tau)\phi_1(\omega, \mu)/\mu\right]\} . \quad (21)$$

Unless otherwise stated, we use the scattering profiles with zero natural line width (cf. eqs. [A6], [A7], and [A11]) in equations (19)–(21). Equations (19) and (20) are three-dimensional integrals. For a representative $N_i(\boldsymbol{k})$, we take

$$N_i(\boldsymbol{k}) \propto \left(\frac{\omega}{\omega_B}\right)^{-1} \Theta(\mu) . \quad (22)$$

The factors in the integrand of equations (19) [(20)] may be viewed pictorially as, from right to left, injection → free-streaming to interaction site → entering block of scatters → exit block of scatters → free-stream and escape by transmission (reflection).

To compare with Monte Carlo calculations of slabs illuminated from "below," we compute the four-dimensional integrals

$$\langle N_T \rangle(\omega) = \frac{1}{\Delta\mu} \int_{\Delta\mu} d\mu\, N_T(\boldsymbol{k}) ; \quad (23)$$

$$\langle N_R \rangle(\omega) = \frac{1}{\Delta\mu} \int_{\Delta\mu} d\mu\, N_R(\boldsymbol{k}) . \quad (24)$$

We evaluate equations (23) and (24) by Gauss quadrature. We find 10-point Gauss quadrature to be sufficient for the τ, μ', and ω' integrals, and 2-point Gauss quadrature sufficient for the (outermost) μ integral. We take the innermost integral to be over ω' since its integrand is sharply peaked. The dominant ω' dependence in the integrand is proportional to $\phi_1(\boldsymbol{k}')\exp\left[-(\tau_0 - \tau)\phi_1(\boldsymbol{k}')/\mu'\right]$, which has at most two maxima satisfying $[1 - (\tau_0 - \tau)\phi_1(\boldsymbol{k}')/\mu']d\phi_1(\boldsymbol{k}')/d\omega' = 0$. We separate the ω' domain into intervals enclosing the maxima and outside the maxima, and apply 10-point Gauss quadrature to each interval.

We plot in Figure 1 the comparison between SAM (dashed lines) and the results from Monte Carlo resonant transfer calculations (solid line) for the transmitted photons. For the purposes of making this comparison, the Monte Carlo code was specifically modified to treat the second and third harmonics as pure absorption lines, i.e., spawning was excluded. For all panels, $B_{12} = 1.71$ and $T = 5$ keV. In Figures (1*a*–1*c*), $0 < \mu < 0.125$ and $N_{e,21} = 0.12$, 1.2, 12, respectively, corresponding to optical depth at the first harmonic of 3, 30, and 300 (cf. eq. [1]; in Fig. 1*c*, $a\tau_1 = 0.4$ so the wings are marginally thin). Figures 1*d*–1*f* repeat Figures 1*a*–1*c* but with $0.25 < \mu < 0.375$, and Figures 1*g*–1*i* repeat Figures 1*a*–1*c* but with $0.75 < \mu < 0.875$. In the simulations, there are $\sim 5 \times 10^4$ photons in Figures 1*a*, 1*d*, 1*g*, and $\sim 2 \times 10^4$ photons in the other panels. Thus, simulation results giving an ordinate of order a few times 10^{-5} (e.g., depth of first harmonic feature in Figure 1*f*) is consistent with a saturated feature (no photons), in agreement with the SAM results.

In Figure 2, we compare the variation with μ of the equivalent widths of the first three harmonics in the transmitted spectra (with spawning excluded) for the SAM (dashed lines) and Monte Carlo (solid lines) models. The equivalent width is defined as

$$EW(\mu) = \int_{E_1}^{E_2} \left[1 - \frac{N_T(\omega, \mu)}{N_i(\omega, \mu)}\right] d\omega , \quad (25)$$

where we take $(E_1, E_2) = (10, 30)$, (30, 50), and (50, 70) keV, respectively, for the first three harmonics. The Monte Carlo equivalent widths have an error of less than $\sim 10\%$, as determined from their variation among different runs. It is evident that the agreement is very good overall. For the first harmonic., the agreement is better than 10%, i.e., within the Monte Carlo statistical errors, except for $\mu < 0.2$ and $N_{e,21} \geq 1.2$, where the difference can be almost a factor of 3. For the second and third harmonics, the agreement is better than 10% when there is a significant feature present. The higher harmonics are optically thin in the region to the right of the vertical bar in Figures 2*b*, 2*c*, 2*e*, 2*f*, 2*h*, and 2*i* (cf. eq. [6]). When $\tau_n^0 \ll 1$ ($n \geq 2$), the equivalent width is simply given by the oscillator strength times the column density, that is, $EW(\mu) \propto N_e(B/B_c)^{n-1}(1 + \mu^2)(1 - \mu^2)^{n-1}/|\mu|$ (cf. Appendix; Lamb et al. 1989). When $\tau_n^0 \gg 1$ (the region to the left of the vertical bar), $EW(\mu) \propto (\ln \tau_n^0)^{1/2}$ (Lamb et al. 1989; Nishimura & Ebisuzaki 1992).

On one hand, as N_e increases, the number of scatters per block increases, which favors complete redistribution. On the other hand, with large N_e, a nonnegligible number of photons which escape into the wings will return to the line core resulting in more than a single block of scatters before escape. The general agreement at the first harmonic indicates, that, to leading order, the single block of scatters transfer picture with complete redistribution is the dominant effect.

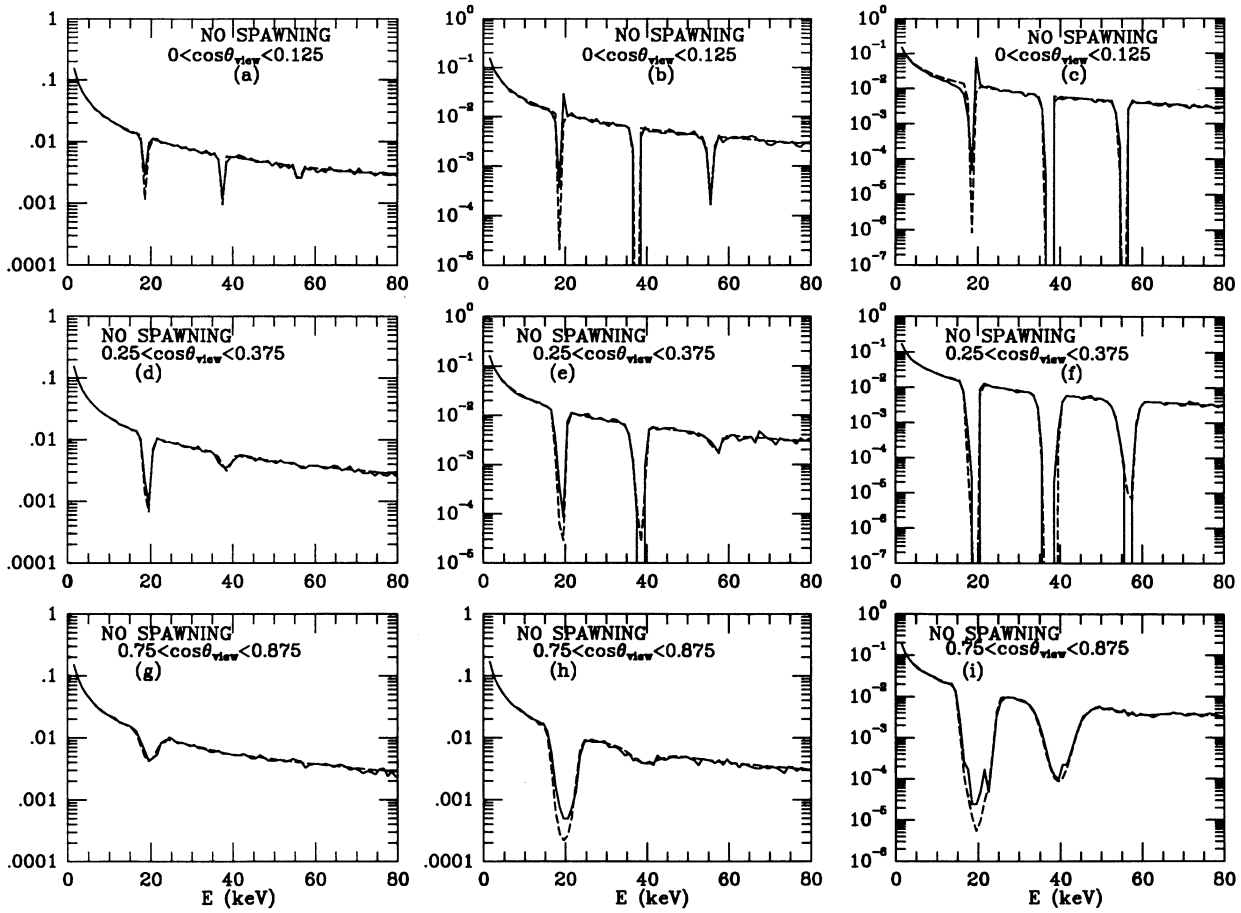

FIG. 1.—The emergent transmitted spectra from the slab with spawning excluded. The magnetic field strength and slab temperature are taken to be $B_{12} = 1.71$ and $T = 5$ keV. Photons are injected isotropically into the slab with a $1/\omega$ spectrum (cf. eq. [22]). The solid lines give the Monte Carlo spectra, the dashed lines give the SAM spectra (cf. eqs. [23] and [19]). For this comparison, the Monte Carlo code was modified to treat the second and third harmonics as pure absorption lines, that is, spawning was turned off. Panels (*a*)–(*c*) show the spectra with $0 < \mu = \cos\theta_{\rm view} < 0.125$ and $N_{e,21} = 0.12$, 1.2, and 12, respectively. Panels (*d*)–(*f*) show the spectra with $0.25 < \mu < 0.375$ and $N_{e,21} = 0.12$, 1.2, and 12, respectively. Panels (*g*)–(*i*) show the spectra with $0.75 < \mu < 0.875$ and $N_{e,21} = 0.12$, 1.2, and 12, respectively. The spectra are normalized to unit area.

As is evident from Figures 1 and 2, SAM is not able to produce the "spike" in the first harmonic feature at low μ and moderate to high N_e. This "spike" which occurs just blueward of the resonant frequency ($\omega_r^0 \approx \omega_B$; see eq. [A8]) in Figures 1*b* and 1*c* arise from the very asymmetric shape of the scattering profile at low values of μ (Lamb et al. 1989)—photons which scatter to frequencies above the μ dependent cutoff ($\approx\omega_B$ at low μ; see eq. [A10]) escapes the slab without any further scattering. Most of the photons in the "spike" come from photons which enter the slab with frequencies just under $\approx\omega_B$ (but with arbitrary μ) and which then scatter into a frequency above the cutoff. This is accomplished in a few scatters since it is relatively easy for these photons to scatter to an energy above $\approx\omega_B$ where a large range of μ values is above the cutoff. At very low N_e, the photons escape more easily by diffusing after a few scatters to the optically thin red wing of the line. As a result, the "spike" becomes progressively weaker at very low N_e (see Fig. 1*a*). The transmitted photons which are born well below the resonant frequency generally escape by diffusing into the optically thin red wing of the line after several scatters, and so contribute little to the "spike"—it is more difficult for these photons to escape by upscattering beyond the cutoff. In contrast, the transmitted photons which are born above the resonant frequency typically escape immediately and therefore do not contribute to the "spike"; that is, they simply form part of the unscattered continuum above the resonance. The SAM formalism assumes the resonant transfer to be a smooth stochastic process unpunctuated by discrete "catastrophic" events, that is, it assumes $q_T(\boldsymbol{k}' \rightarrow \boldsymbol{k}, \tau)$ and $q_R(\boldsymbol{k}' \rightarrow \boldsymbol{k}, \tau)$ to be smooth continuous functions. This assumption is violated when photons escape abruptly into the "spike" by scattering above the cutoff frequency.

For comparison, we have also run SAM models using scattering profiles with *finite* natural line width (i.e., finite "a"; cf. Appendix, eqs. [A6], [A14], and [A15]) for both cases with and without spawning included (see § 3). As expected, for sufficiently low column depths, the results are similar to the models using zero line width profiles. For $N_{e,21} \lesssim 1$, the difference in the equivalent widths of the first three harmonics is generally less than 10% between the SAM models using profiles with zero and finite line width, except for the lowest angular (μ) bin where the difference can be a factor of 3 or more. This discrepancy in the lowest μ bin is due to the difference between the zero and finite line width profiles above the cutoff frequency (cf. Appendix) which become increasingly pronounced as $\mu \rightarrow 0$. For $N_{e,21} \sim 10$, the difference in the equivalent widths of the first three harmonics between the SAM models

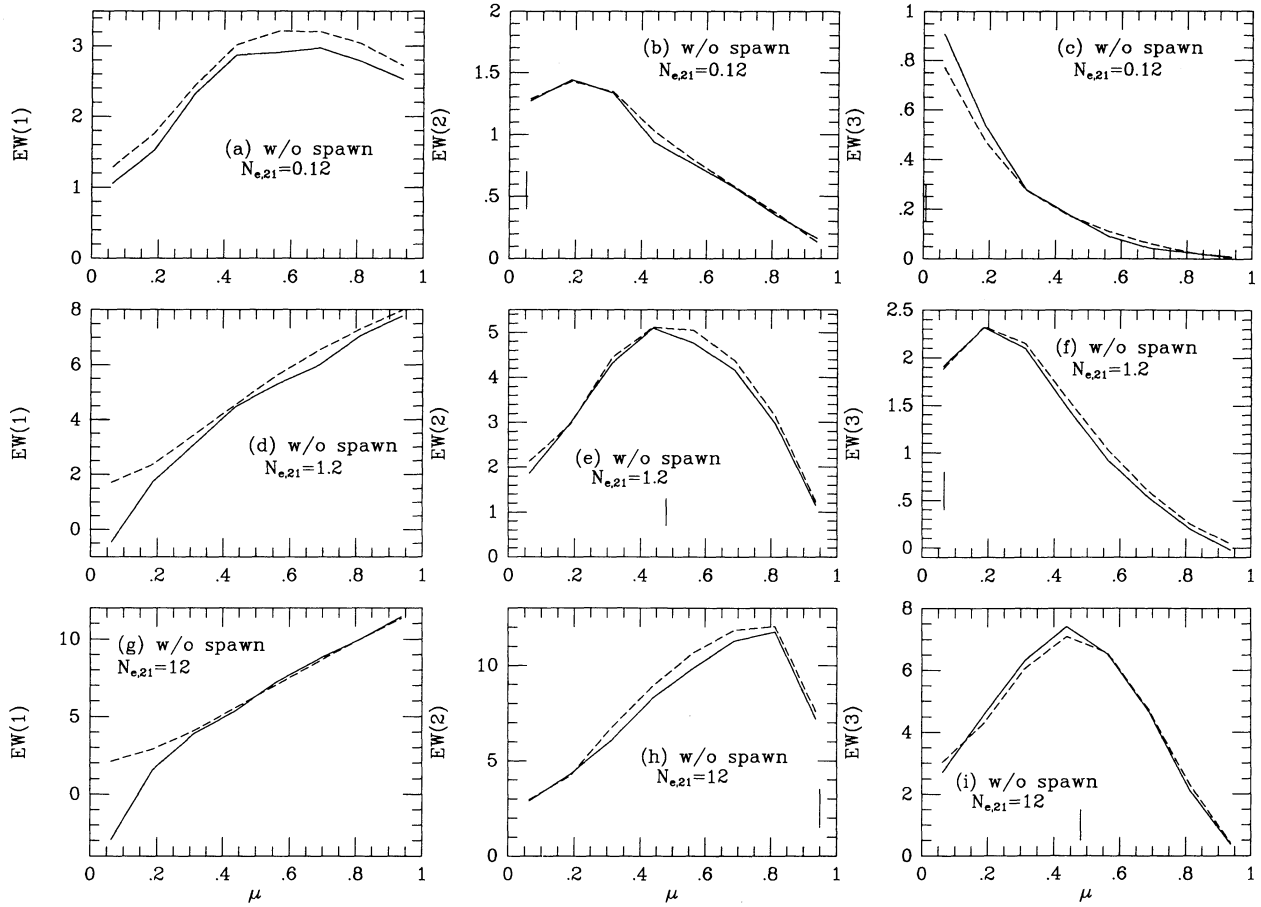

FIG. 2.—The equivalent width (EW) of the first three harmonics as a function of μ determined from the spectra in Figure 1. Panels (*a*)–(*c*) give the EW for the first three harmonics for $N_{e,21} = 0.12$. Panels (*d*)–(*f*) give the EW for the first three harmonics for $N_{e,21} = 1.2$. Panels (*g*)–(*i*) give the EW for the first three harmonics for $N_{e,21} = 12$. The second harmonic is optically thin ($\tau_2^0 < 1$, cf. eq. [6]) to the right of the vertical bar in panels (*b*), (*e*), and (*h*). The third harmonic is optically thin ($\tau_3^0 < 1$, cf. eq. [6]) to the right of the vertical bar in panels (*c*), (*f*), and (*i*).

using zero and finite line width profiles is generally less than 30% (except in the lowest μ bin). At this depth, the wings are becoming significant (cf. eq. [3]), so larger differences are expected.

We plot in Figure 3 the comparison between SAM reflected spectra (dashed lines) and the corresponding results from Monte Carlo calculations (solid lines). The Monte Carlo simulations include (magnetic) continuum scattering, so the reflected spectra contain photons outside the resonant first harmonic bump, their numbers increasing as N_e increases. Nevertheless, their numbers remain negligible in comparison to the numbers of photons at the first harmonic as long as the first harmonic optical depth is modestly optically thick (cf. eq. [2]). The SAM reflected component includes only the resonant scattering contribution from the first harmonic, and so continuum-scattered photons are absent in the dashed curves.

3. FIRST HARMONIC WITH SPAWNING

We now introduce spawning into SAM. We obtain an estimate of the importance of spawning by comparing the number of first harmonic photons produced from spawning at the second harmonic (N_2), with the number of nonspawned first harmonic photons that experience resonant scattering (N_1). In weak fields (that is, $B/B_c \ll 1$), when a second harmonic photon Raman scatters, the dominant scattering channel produces two outgoing first harmonic photons. Thus, crudely,

$$\frac{N_2}{N_1} \approx \frac{2N_i(2\omega_B)(2\omega_D)\tau_2}{N_i(\omega_B)\omega_D\sqrt{\ln\tau_1}}, \tag{26}$$

where $N_i(\omega)$ is the spectral distribution of the photons injected into the slab. With $N_i(\omega) \propto 1/\omega$, we have

$$\frac{N_2}{N_1} = \frac{2\tau_2}{\sqrt{\ln\tau_1}} \sim \tau_2 .$$

As a result, spawning becomes significant when $\tau_2 \gtrsim 1$, that is, when $N_{e,21} \gtrsim 0.7(T/\mathrm{keV})^{1/2}$ (see eq. [4]).

We consider here only the effect of spawning from the second harmonic; the generalization to higher harmonics is straightforward. The number of third harmonic spawning events, S_3, compared with the number of second harmonic spawning events, S_2, is

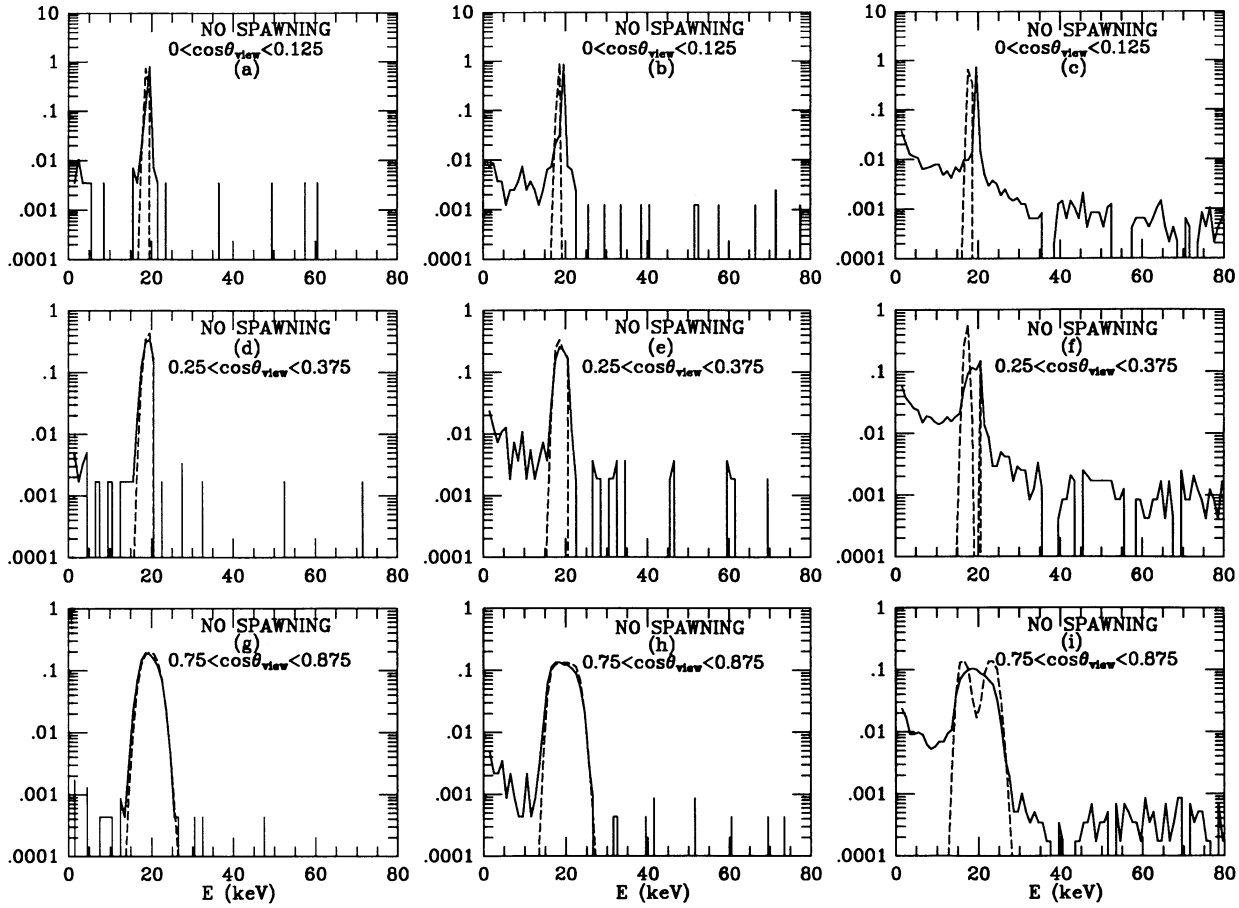

FIG. 3.—The emergent reflected spectra from the slab with spawning excluded. The parameters and manner of display are the same as for Fig. 1. The SAM results are obtained from eqs. (24) and (20).

given by

$$\frac{S_3}{S_2} \sim \begin{cases} \dfrac{\tau_3}{\tau_2}, & \tau_3 \ll \tau_2 \ll 1; \\ \dfrac{\tau_3}{\sqrt{\ln \tau_2}}, & \tau_3 \ll 1 \ll \tau_2, \end{cases} \tag{27}$$

for $N_i(\omega) \propto 1/\omega$. We therefore expect spawning from the third harmonic to become significant when $\tau_3 \gtrsim 1$, that is, when $N_{e,21} \gtrsim 12 B_{12}^{-1} (T/\mathrm{keV})^{1/2}$ (cf. eq. [5]).

When $B/B_c \ll 1$, interactions at the second (and higher harmonics) mainly produce first harmonic photons, with the strength of this source proportional to $N_i(\boldsymbol{k})$. These new first harmonic photons then experience multiple resonant scatters before escape. The production profile as a function of τ inside the slab for spawning from second harmonic photons is given by

$$s(\tau) = \int_{\mu' > 0} d\boldsymbol{k}' \phi_2(\boldsymbol{k}') \frac{\exp\left[-(\tau_0 - \tau)\phi_2(\boldsymbol{k}')/\mu'\right]}{\mu'} N_i(\boldsymbol{k}') , \tag{28}$$

where $\phi_2(\boldsymbol{k})$ is the resonant scattering profile at the second harmonic. Pictorially, the factors in the integrand in equation (28) give, from right to left, injection into slab → free streaming to τ → interaction (spawning) at τ. We compare in Figure 4 the spawning profile obtained from equation (28) (solid curve) with that obtained from Monte Carlo simulations. The Monte Carlo simulations include spawning from the second and third harmonics; the dashed histogram shows the spawning contribution from only second harmonic photons and the solid histogram shows the total spawning contribution from both second and third harmonic photons. Figures 4*a*–4*c* give the profile inside the slab for $N_{e,21} = 0.12$, 1.2, and 12, respectively. Photons are injected into the "bottom" side of the slab at $\tau/\tau_0 = 1$, and they escape by transmission from the "top" side of the slab at $\tau/\tau_0 = 0$. It is evident that for $N_{e,21} \lesssim 10$, spawning from the third harmonic is not significant, as expected.

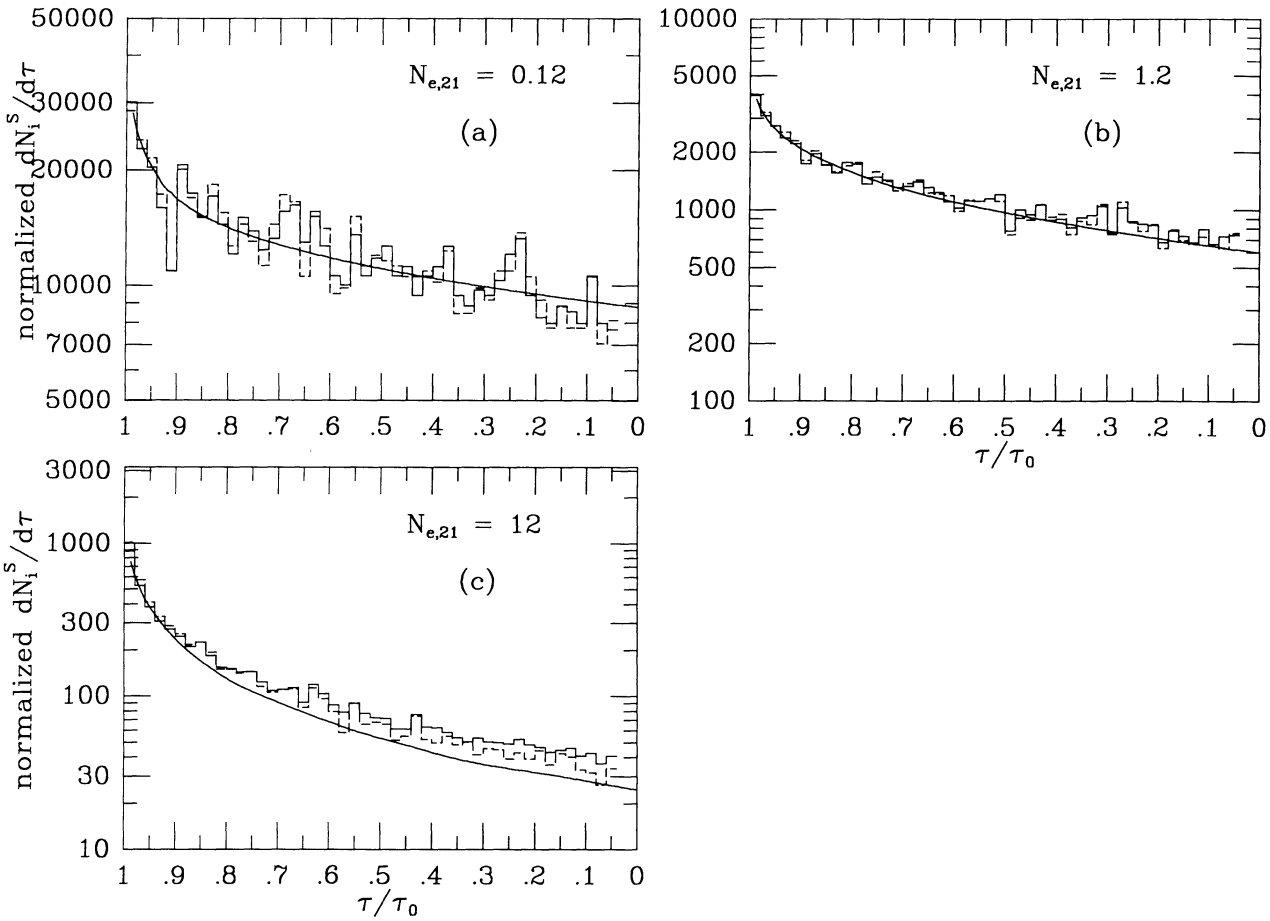

FIG. 4.—The spawning profile inside the slab for $N_{e,21} = (a)$ 0.12, (b) 1.2, and (c) 12. Photons enter the slab from the left ($\tau/\tau_0 = 1$). The dashed histogram gives the (Monte Carlo) spawning contribution from second harmonic photons, the solid histogram gives the total spawning contribution from second and third harmonic photons. The solid curve is obtained from eq. (28). The profiles are normalized to unit area.

We assume each spawning from the second harmonic produces two photons with identical properties $\boldsymbol{k}$. The emissivity for spawned photons (in photons $\mathrm{cm}^{-2}\,\mathrm{s}^{-1}\,\mathrm{keV}^{-1}\,\mathrm{sr}^{-1}$), is then given by

$$N_i^S(\boldsymbol{k}, \tau) = 2 \times \tfrac{3}{8}(1 + \mu^2) f(\omega) s(\tau)\,, \tag{29}$$

where (ω, μ) are the energy and direction cosine, respectively, of the spawned photons, and $\int f(\omega) d\omega = 1$. The transmitted ($\mu > 0$) photon intensity is then given by

$$\begin{aligned} N_T(\boldsymbol{k}) = {} & N_i(\boldsymbol{k}) \exp\left[\frac{-\tau_0\,\phi(\boldsymbol{k})}{\mu}\right] + \int_0^{\tau_0} d\tau \int_{\mu'>0} d\boldsymbol{k}' q_T(\boldsymbol{k}' \to \boldsymbol{k}, \tau) \phi_1(\boldsymbol{k}') \frac{\exp\left[-(\tau_0 - \tau)\phi_1(\boldsymbol{k}')/\mu'\right]}{\mu'} N_i(\boldsymbol{k}') \\ & + \int_0^{\tau_0} d\tau' N_i^S(\boldsymbol{k}, \tau') \exp\left[\frac{-\tau'\phi_1(\boldsymbol{k})}{\mu}\right] + \int_0^{\tau_0} d\tau \int_\tau^{\tau_0} d\tau' \int_{\mu'>0} d\boldsymbol{k}' q_T(\boldsymbol{k}' \to \boldsymbol{k}, \tau) \phi_1(\boldsymbol{k}') \frac{\exp\left[-(\tau' - \tau)\phi_1(\boldsymbol{k}')/\mu'\right]}{\mu'} N_i^S(\boldsymbol{k}', \tau') \\ & + \int_0^{\tau_0} d\tau \int_0^{\tau} d\tau' \int_{\mu'<0} d\boldsymbol{k}' q_T(\boldsymbol{k}' \to \boldsymbol{k}, \tau) \phi_1(\boldsymbol{k}') \frac{\exp\left[-(\tau' - \tau)\phi_1(\boldsymbol{k}')/\mu'\right]}{|\mu'|} N_i^S(\boldsymbol{k}', \tau')\,, \end{aligned} \tag{30}$$

and the reflected ($\mu < 0$) photon intensity is given by

$$\begin{aligned} N_R(\boldsymbol{k}) = {} & \int_0^{\tau_0} d\tau \int_{\mu'>0} d\boldsymbol{k}' q_R(\boldsymbol{k}' \to \boldsymbol{k}, \tau) \phi_1(\boldsymbol{k}') \frac{\exp\left[-(\tau_0 - \tau)\phi_1(\boldsymbol{k}')/\mu'\right]}{\mu'} N_i(\boldsymbol{k}') + \int_0^{\tau_0} d\tau' N_i^S(\boldsymbol{k}, \tau') \exp\left[\frac{-(\tau' - \tau_0)\phi_1(\boldsymbol{k})}{\mu}\right] \\ & + \int_0^{\tau_0} d\tau \int_\tau^{\tau_0} d\tau' \int_{\mu'>0} d\boldsymbol{k}' q_R(\boldsymbol{k}' \to \boldsymbol{k}, \tau) \phi_1(\boldsymbol{k}') \frac{\exp\left[-(\tau' - \tau)\phi_1(\boldsymbol{k}')/\mu'\right]}{\mu'} N_i^S(\boldsymbol{k}', \tau') \\ & + \int_0^{\tau_0} d\tau \int_0^{\tau} d\tau' \int_{\mu'<0} d\boldsymbol{k}' q_R(\boldsymbol{k}' \to \boldsymbol{k}, \tau) \phi_1(\boldsymbol{k}') \frac{\exp\left[-(\tau' - \tau)\phi_1(\boldsymbol{k}')/\mu'\right]}{|\mu'|} N_i^S(\boldsymbol{k}', \tau')\,, \end{aligned} \tag{31}$$

where q_T and q_R are given by equations (14) and (15), respectively. Setting $\phi(\boldsymbol{k}) = \phi_1(\boldsymbol{k})$ in equation (30), it is easily shown by virtue of equation (12) that

$$\int d\boldsymbol{k}[N_T(\boldsymbol{k}) + N_R(\boldsymbol{k})] = \int d\boldsymbol{k} N_i(\boldsymbol{k}) + \int d\boldsymbol{k} \int_0^{\tau_0} d\tau\, N_i^S(\boldsymbol{k}, \tau) \tag{32}$$

(cf. eq. [13]). We note here that the general form of the transmitted and reflected intensity for *arbitrary* emissivity $N_i^{\rm gen}(\boldsymbol{k}, \tau)$ is given by the last three terms in equations (30) and (31), respectively, with $N_i^S \to N_i^{\rm gen}$.

To compare with Monte Carlo simulations, we compute $\langle N_T \rangle$ and $\langle N_R \rangle$ from equations (30) and (31). We use two different forms for $f(\omega)$

$$f(\omega) = \delta(\omega - \omega_{\rm sp})\,, \tag{33}$$

$$f(\omega) = \frac{\exp\{-[(\omega - \omega_{\rm sp})/\omega_{\rm D}\mu]^2\}}{\omega_{\rm D}\sqrt{\pi}|\mu|}\,, \tag{34}$$

where $\omega_{\rm sp}/m_e \equiv (1/2)[(1 + 4B/B_c)^{1/2} - 1]$. Equation (34) is a fair approximation to the actual energy distribution of the spawned photons at birth, as shown in Figure 5, where we plot this distribution for a slab with $N_{e,21} = 1.2$. The solid histogram gives the distribution for photons born with $\mu > 0$, while the dashed histogram gives those born with $\mu < 0$. The solid curve is equation (34).

For computing $\langle N_T \rangle$ and $\langle N_R \rangle$, there is a very small difference (roughly a few percent) between using equations (33) and (34). This is true so long as $f(\omega)$ is a strongly peaked function ($\omega_{\rm D}/\omega_B \ll 1$)—which it generally is. The difference in computational speed is, however, substantial; the Gaussian approximation involves five-dimensional integrals for the spawning contributions, while only four-dimensional integrals are required using the delta function approximation. All SAM results with spawning presented in this paper are obtained using equation (33). Since the resultant four-dimensional integrals from the spawning contributions do not involve integrals over ω', the most time consuming computation comes from evaluating the four-dimensional integrals from the no-spawn contributions (cf. eqs. [19] and [20]).

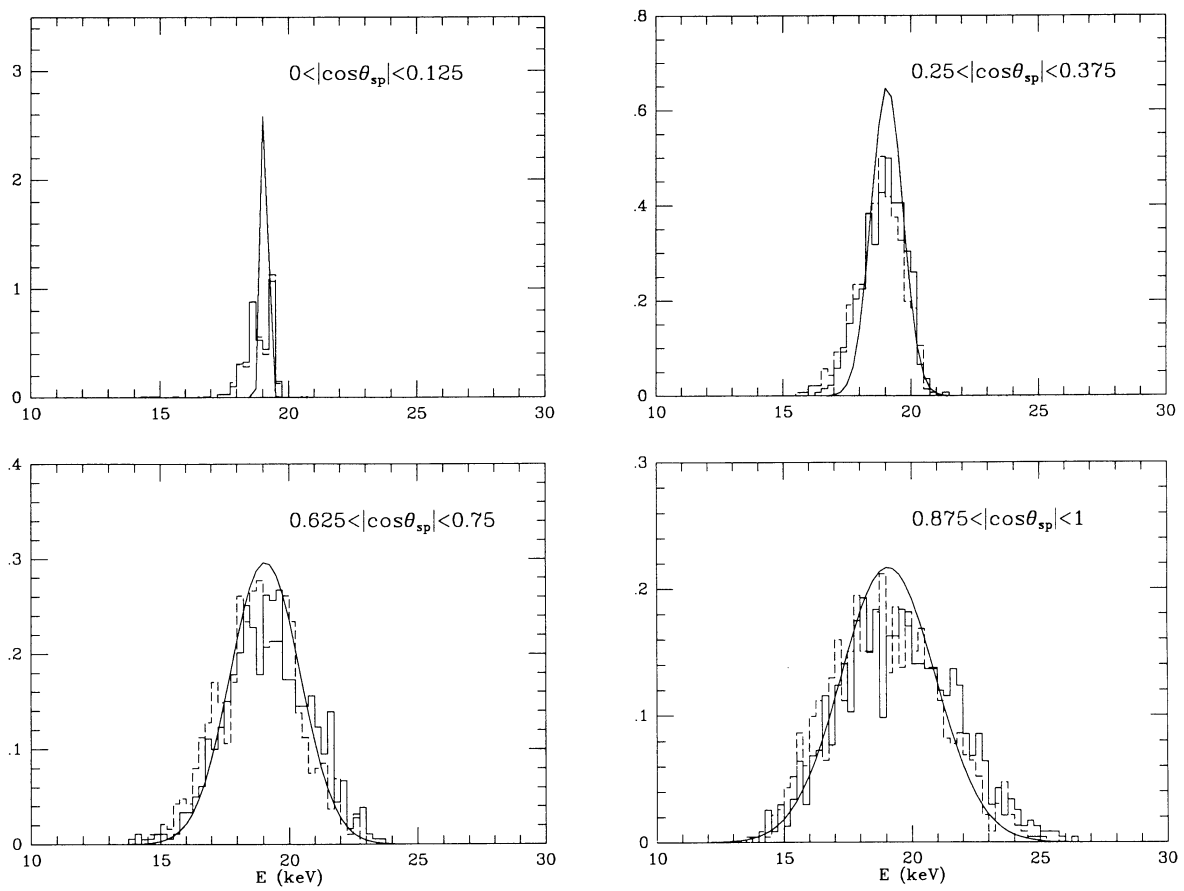

FIG. 5.—Representative frequency profiles of spawned photons at "birth" inside the slab. The spawned photon's direction cosine is denoted cos $\theta_{\rm sp}$. The solid (*dashed*) histogram gives the Monte Carlo distribution of spawns produced with cos $\theta_{\rm sp} > 0$ (< 0). The solid curve is the Gaussian approximation given by eq. (34). The profiles are normalized to unit area. It is worth noting here that unlike discrete methods, the Monte Carlo simulations track photons continuously in angle and frequency.

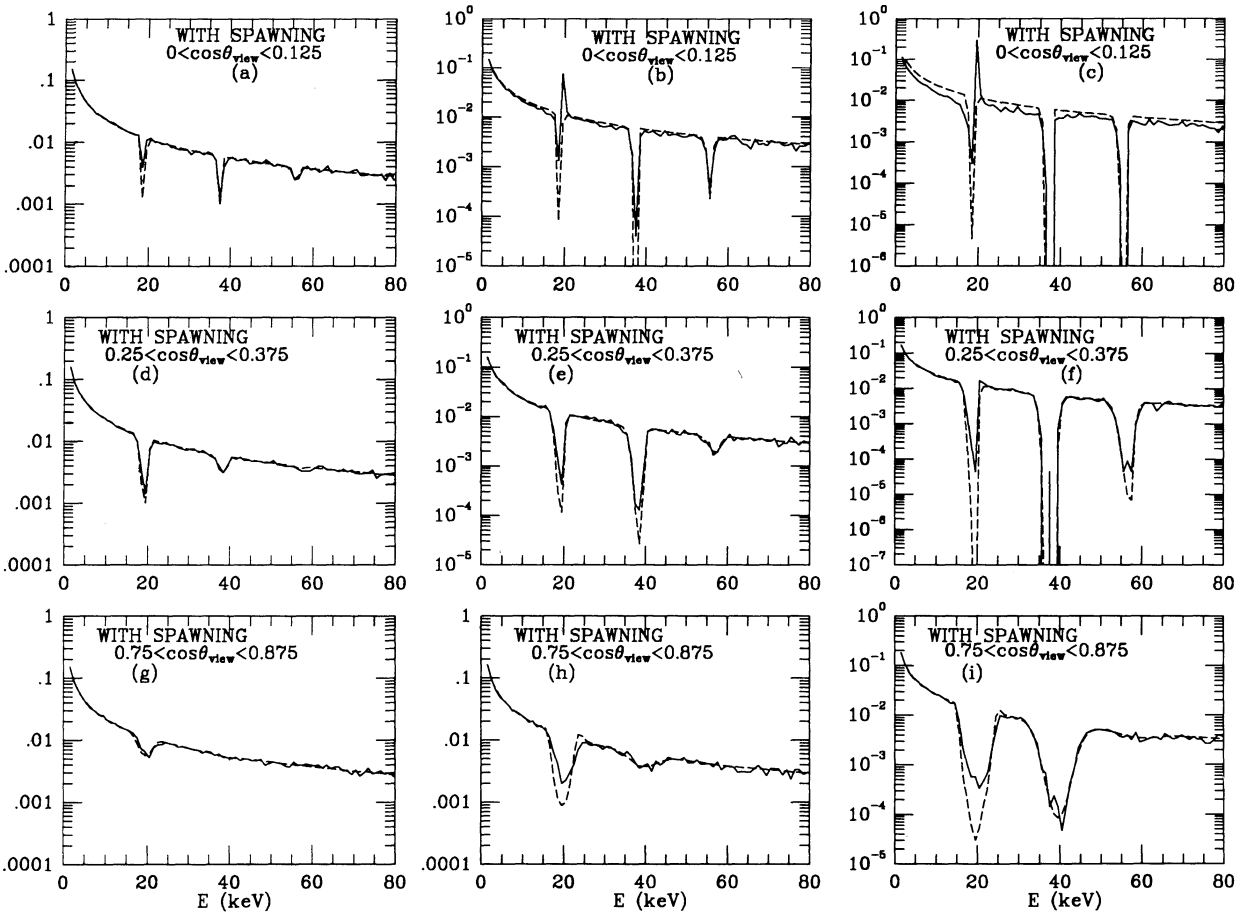

FIG. 6.—The emergent transmitted spectra from the slab with spawning included. The parameters and manner of display are the same as for Fig. 1. The SAM results are obtained from eqs. (23) and (30). The spectra are normalized to unit area, which causes the relative shift in the curves in panels (*b*) and (*c*).

We plot in Figure 6 the comparison between SAM (dashed lines) and Monte Carlo simulations including spawning (solid line) for the transmitted photons. The parameters for the panels are the same as in Figure 1. The SAM includes spawning from the second harmonic only and treats the second and third harmonics as pure absorption features. The Monte Carlo simulations treat all first three harmonics as scattering lines and includes spawning from both the second and third harmonics.

In Figure 7, we compare the variation with μ of the equivalent widths of the first three harmonics in the transmitted spectra (with spawning included) for the SAM (dashed lines) and Monte Carlo (solid lines) models. As remarked earlier, because of the high branching ratio for spawning, pure absorption is an excellent approximation for the higher harmonics and for them the equivalent widths agree to better than 10%. For the first harmonic, the agreement is good (typically $<20\%$) for $\mu > 0.2$, but, as with the no-spawn case, the SAM cannot produce the spike at low μ and moderate to high N_e. This spike is enhanced by the presence of spawning, especially at high N_e, and can give rise to a "true emission" feature (i.e., negative equivalent width; see Figures 6*b*–6*c*).

We plot in Figure 8 the comparison between SAM reflected spectra (dashed lines) and the corresponding results from Monte Carlo calculations (solid lines). The bumps at the second and, less noticeably, third, harmonics in the Monte Carlo spectra come from the small fraction $[\sim(B/B_c)^{2(n-1)}, n \geq 2]$ of second and third harmonic photons that did not suffer spawning during an interaction but escaped after a single scatter. The higher harmonic scattering has the angular dependence given by $\sin^{2n-2}\theta'(1+\cos^2\theta')\sin^{2n-2}\theta(1+\cos^2\theta)$, with $(\mu', \mu) = (\cos\theta', \cos\theta)$ the (incident, scattered) direction cosine, and so favors scattering orthogonal to the field. As a result, the bumps are prominent at low μ and low N_e (see, e.g., Figs. 8*a* and 8*d*). At high N_e, the photons that scatter into low μ will likely interact again and be destroyed, since it is extremely unlikely $[\sim(B/B_c)^{4(n-1)}]$ for a photon to survive two successive scatters without spawning. The bumps at low μ are therefore suppressed at large N_e (see, e.g., Fig. 8*c*). Photons rarely scatter into high μ, but if they do, they tend to escape readily, even for large N_e (see, e.g., Figs. [8*g*–8*i*]); in Fig. 8*i* photons escaping by magnetic continuum scattering begin to swamp the higher harmonic bumps). We have included only the first harmonic in the SAM calculations, and so the higher harmonic bumps are absent in the dashed curves. These higher harmonic bumps may be modeled as single scatter features with allowance for suppression at large N_e and small μ.

4. DISCUSSION AND CONCLUSIONS

We have devised a semi-analytic model (SAM) for the formation of cyclotron lines in weak fields ($B/B_c \ll 1$) and in static media that is optically thick in the core of the first harmonic but optically thin in its wings (see eqs. [2], [3]). In this formalism, the

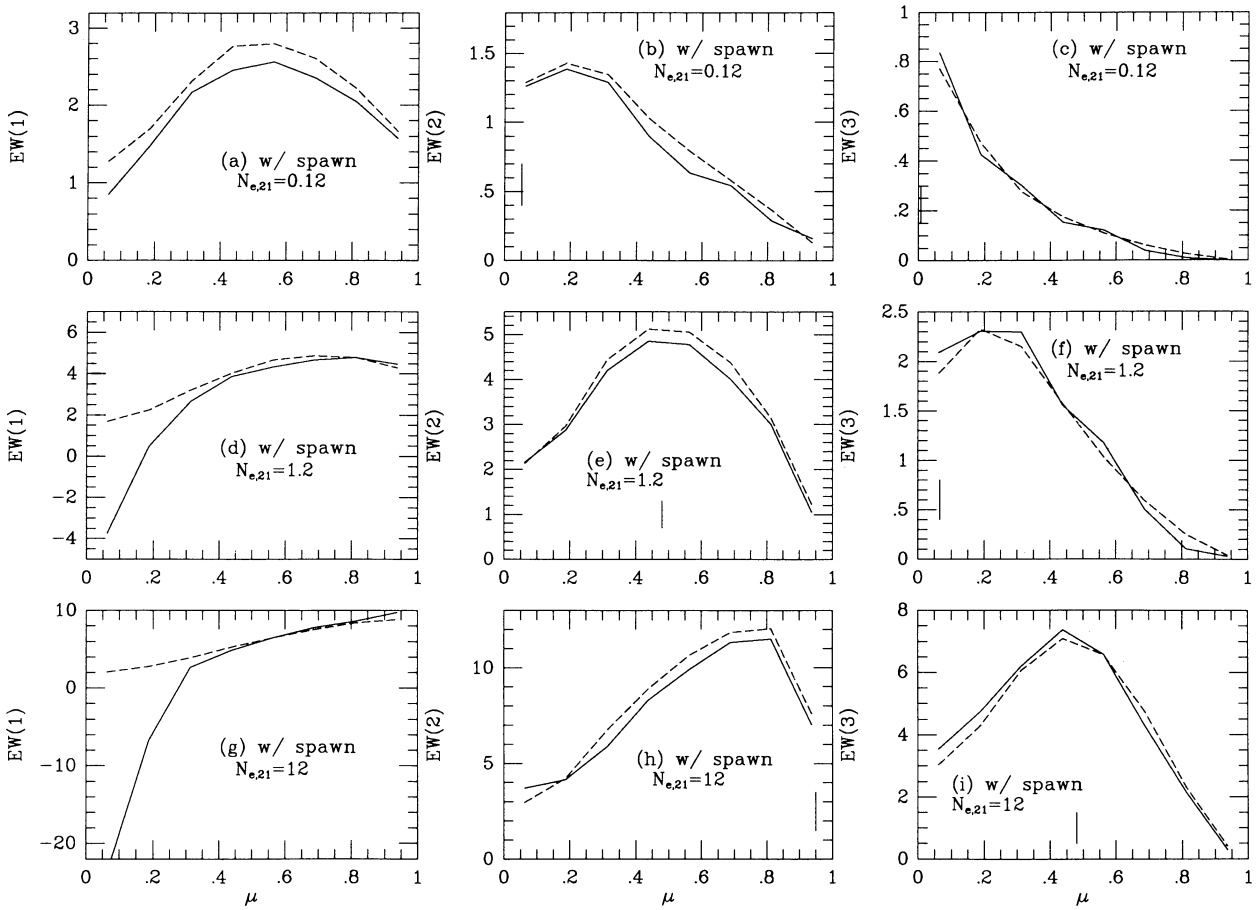

FIG. 7.—The equivalent width (EW) of the first three harmonics as a function of μ determined from the spectra in Fig. 6. The manner of display is the same as for Fig. 2.

emergent spectral shape is reduced to quadratures. The general formalism for plane-parallel geometry is embodied in equations (8)–(16) and (30)–(32). We view the formation of the first harmonic feature as the result of a single block of resonant photon scatters in the line core. The central assumption here is that the properties of the photons emerging from the scattering block are uncorrelated with those of the photons entering the scattering block; that is, complete redistribution applies to the single *block* of scatters. Spawning from higher harmonics is incorporated by modifying the emissivity $N_i(\boldsymbol{k})$ in equations (10) and (11) (cf. eqs. [30]–[32]). The higher harmonics themselves are modeled as true absorption features.

We illustrate the SAM by specializing to unpolarized transfer through a slab that is threaded by a uniform magnetic field oriented parallel to the slab normal. One possible application is to modeling the low-energy absorption-like features that have been seen in the spectra of several classical γ-ray bursts (Fenimore et al. 1988; Lamb et al. 1989; Alexander & Mészáros 1989; Wang et al. 1989b). Since the first harmonic line wings are assumed to be optically thin, we use the scattering profiles with zero natural line width (but including relativistic kinematics; cf. Appendix). We also incorporate spawning from the second harmonic into the SAM (see § 3; eqs. [28]–[34]). Inclusion of higher harmonics essentially entails the addition of additional terms to $N_i(\boldsymbol{k})$ and $N_i^S(\boldsymbol{k}, \tau)$ to describe the additional sources of first *and* higher harmonic photons. For instance, to leading order, the spawning of first harmonic photons from a third harmonic photon involves direct production of three first harmonic photons from an interaction. This involves adding to equation (29) a similar term with $2 \times \frac{3}{8} \rightarrow 3 \times \frac{3}{8}$ and with $\phi_2 \rightarrow \phi_3$ and $w_{sp}/m_e = (1/3)[(1 + 6B/B_c)^{1/2} - 1]$ (see eqn. [28], [33], and [34]). The production of a second harmonic photon from a third harmonic photon which in turn spawn two first harmonic photons is a higher order process in B/B_c (although the final result is still three first harmonic photons).

The SAM spectral features agree well in position, shape, and equivalent width with the Monte Carlo results except, for moderate to high N_e, at large viewing angles (low μ) relative to the field (see Figures 1, 2, 3, 6, 7, and 8). First harmonic photons that scatter into low μ blueward of the relativistic cutoff frequency in the scattering profile ($\approx \omega_B$) can escape the slab immediately, thereby forming an emission "spike" blueward of line center (cf. Figs. 1*b*, *c*; 6*b*, *c*). Since SAM treats the resonant transfer as a continuous stochastic process, it cannot model these discrete "catastrophic" events that give rise to the "spikes" (see § 2).

The number of photons in a Monte Carlo simulation needed for good signal-to-noise spectra suitable for direct comparison with observed spectra (i.e., $\delta\chi^2 \sim 1$ between comparisons using different simulations) is $\approx 10^6$. At $N_{e,21} = 1.2$, such a simulation takes $\sim$800 seconds on a Cray YMP, or $\sim$4000 s on a Silicon Graphics SG280. To cover eight μ values, the SAM with δ-function spawning (cf. § 3, eq. [33]) takes $\sim$100 s on the YMP and $\sim$400 seconds on the SG280. Each Monte Carlo simulation gives "for

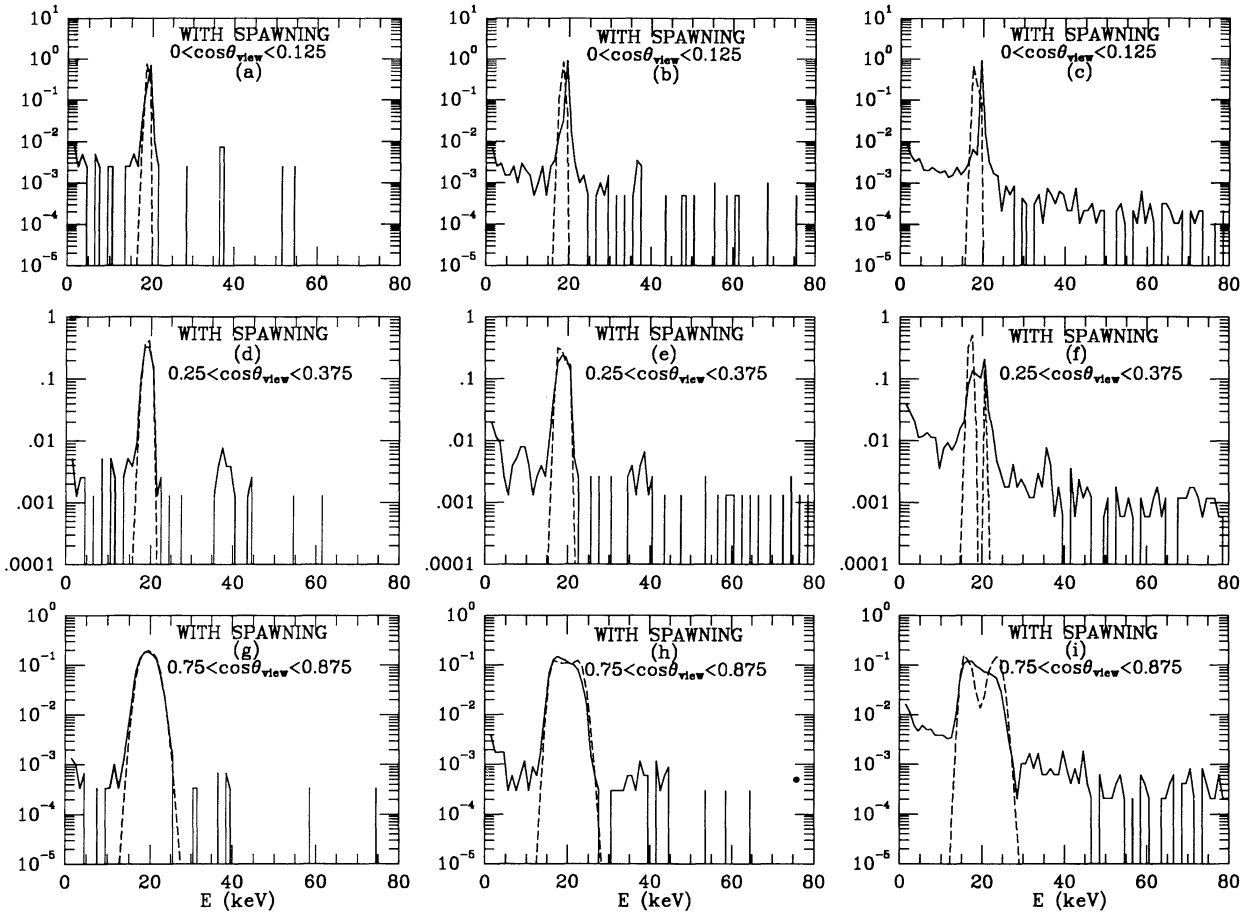

FIG. 8.—The emergent reflected spectra from the slab with spawning included. The parameters and manner of display are the same as for Fig. 1. The SAM results are obtained from eqs. (24) and (31). Bumps at higher harmonics are absent from the SAM curves because eq. (31) treats only the first harmonic.

free" the spectral binning in μ, whereas SAM requires a separate evaluation for each μ. On the other hand, the time required for SAM is relatively constant with N_e, while the time required for each Monte Carlo simulation rises appreciably with increasing N_e (roughly as $N_e^{0.4}$). The SAM is therefore at least an order of magnitude faster to compute than Monte Carlo. As such, it becomes feasible to use the SAM as a *physical* model for directly fitting large numbers of γ-ray burst line spectra once they become available.

Since the SAM is based upon only a few simple physical principles—the transfer as a smooth stochastic process, complete redistribution in a single block of scatters for the first harmonic, "true" absorption for the higher harmonics—it should be easily adaptable to more general physical situations. Combined with its speed, it therefore offers the promise of liberating researchers from large codes and time consuming simulations in their analysis of cyclotron line spectra.

An immediate potential generalization is to the formation of cyclotron lines in dynamic media of moderate depth. The recent observations of the isotropy of the classical γ-ray bursts by the *CGRO* (Meegan et al. 1992) rules out a pure Galactic disk origin for these events. If the bursts have a Galactic origin, then the bulk of these events may arise from neutron stars which reside in an extended halo (>30 kpc; e.g., Brainerd 1992; Wasserman 1992). LWW showed that line formation models with static line forming regions are constrained by the cyclotron-line–enhanced Eddington flux to have the source lie within a few hundred parsecs from the Sun (for example, they obtain a bound of ~ 200 pc for GB 880205). As a result, these static models may not be applicable to the bulk of the bursts that display line features in their low-energy spectra. This constraint, however, does not apply to models where the lines form in dynamic media. One such model was put forward by Miller et al. (1991) who proposed that the low-energy absorption-like features seen in the classical γ-ray bursts such as GB 880205 were cyclotron line features formed in a relativistically expanding $e^{\pm}$ pair wind. They were able to successfully model the second harmonic seen in a spectrum of GB 880205, but have not been able to treat the formation of the first harmonic feature. We are currently extending the SAM formalism to treat line formation, in particular, the formation of the first harmonic feature, in dynamic media.

The SAM model discussed in this work involves a single scattering block. A potential extension would be to include a weighted sum over *multiple* scattering blocks using finite line width profiles. This transfer picture applies to media where the first harmonic line wings are optically thick. In these media, multiple resonant photon scatters in the line *wings* return the photon to the core several times before the photon finally escapes in the wings (cf. Wasserman & Salpeter 1980). Such optically thick media is believed to be realized in the line forming regions in accretion-driven magnetized X-ray pulsars such as Her X-1. We shall defer this extension of SAM to a future paper.

APPENDIX

THE RELATIVISTIC SCATTERING PROFILE

The energy level of the nth Landau level is

$$\omega_n = (1 + 2nb)^{1/2} - 1 , \tag{A1}$$

where $b \equiv B/B_c$ ($B_c = m^2/e = 4.414 \times 10^{13}$ G). We use units where $\hbar = c = k_B = m_e = 1$ throughout this Appendix. The dimensionless scattering profile for the nth harmonic is defined as

$$\phi_n(\omega, \mu) = \int_{-\infty}^{+\infty} dp f(p)(1 - \beta\mu)\left\langle \frac{\sigma_n}{\sigma_T} \right\rangle_r , \tag{A2}$$

where

$$\left\langle \frac{\sigma_n}{\sigma_T} \right\rangle_r = c_n(1 + \mu_r^2)(1 - \mu_r^2)^{n-1}\delta(E_i^r - E_f^r) \tag{A3}$$

is the weak field ($n^2 b \ll 1$) polarization-averaged resonant scattering cross section in the electron rest frame for the nth harmonic, and $\sigma_T = 6.65 \times 10^{-25}$ (cm^2) is the Thomson cross section. The subscript (superscript) r denote a quantity measured in the electron rest frame. The δ-function prescribes energy conservation for the resonant absorption that initiates the resonant scattering. In equation (A3), $\theta_r = \cos^{-1}\mu_r$ is the photon propagation angle with respect to the magnetic field,

$$c_n = c_0 b^{n-1}\frac{(n^2/2)^{n-1}}{(n-1)!} , \qquad c_0 = \frac{3}{8}\frac{\pi}{e^2} \approx 161.442 , \tag{A4}$$

$$E_i^r - E_f^r = 1 + \omega_r - (1 + \omega_r^2\mu_r^2 + 2nb)^{1/2} ,$$

$$f(p) = \frac{1}{2K_1\left(\frac{1}{T}\right)} \exp\left\{ -\left[\frac{(p^2 + 1)^{1/2} - 1}{T}\right]\right\} , \qquad K_1(1/T) = \int_0^\infty dx \exp\left\{ -\left[\frac{(x^2 + 1)^{1/2} - 1}{T}\right]\right\} , \tag{A5}$$

and $\omega_r = \gamma\omega(1 - \beta\mu)$ with $\gamma = (1 + p^2)^{1/2}$ the incident photon energy. For an isothermal slab with an electron column density N_e, the polarization averaged optical depth for the nth harmonic is given by $\tau_n(\omega, \mu) = \sigma_T N_e \phi_n(\omega, \mu)$.

Adopting zero natural line width, the scattering profile for $|\mu| \neq 1$ becomes

$$\phi(\omega, \mu) = \sum_{n=1}^{n_{max}} \sum_{j=\pm} \phi_n(p_j; \omega, \mu) , \tag{A6}$$

where

$$\phi_n(p_j; \omega, \mu) = \frac{c_n}{\omega} f(p_j) \frac{(1 + \mu_{r,j}^2)(1 - \mu_{r,j}^2)^{n-1}}{|\mu_{r,j}|}(1 + \omega_{r,j}^0) , \tag{A7}$$

$$\mu_{r,j} = \frac{\mu - \beta_j}{1 - \beta_j\mu} , \qquad \beta_j = \frac{p_j}{\gamma_j} = \frac{p_j}{\sqrt{1 + p_j^2}} ;$$

$$\omega_{r,j}^0 = \frac{2nb}{1 + [1 + 2nb(1 - \mu_{r,j}^2)]^{1/2}} \tag{A8}$$

is the resonant absorption frequency in the rest frame. The two resonant momenta (the roots of $E_i^r - E_f^r = 0$) are given by

$$p_\pm = \frac{\mu[2nb - \omega^2(1 - \mu^2)] \pm (1 - \mu^2)[(\omega^2 - \omega_-^2)(\omega^2 - \omega_+^2)]^{1/2}}{2\omega(1 - \mu^2)} , \tag{A9}$$

where

$$\omega_\pm = \frac{\sqrt{1 + 2nb} \pm 1}{\sqrt{1 - \mu^2}} , \tag{A10}$$

and $0 \leq \omega \leq \omega_- < \omega_+$. The roots for $\omega > \omega_+$ are spurious. The frequency ω_- is the cutoff frequency referred to in the text (end of § 2). The profile vanishes above this cutoff frequency and it gives rise to the asymmetric shape of the profiles which are prominent at low values of μ (cf. Lamb et al. 1989). This cutoff frequency is a purely relativistic kinematical effect and may be understood as follows.

Consider a frame K where an electron moves with velocity u along a field line and a photon is incident with frequency ω and direction cosine μ. Now boost to the frame K' where the photon is traveling orthogonal to the field. The required boost is given by

$\mu' = (\mu - \beta)/(1 - \beta\mu) = 0$, or $\beta = \mu$. In K', the electron moves with velocity $u' = (u - \beta)/(1 - u\beta)$. The resonant condition $\omega_r = \omega_r^0$ expressed in frame K' is $\omega_r = \gamma'\omega'(1 - u'\mu') = \gamma'\omega' = \omega_r^0$, with $\gamma' = (1 - u'^2)^{-1/2}$. Boosting from K' to the electron rest frame, we have $\mu_r = (\mu' - u')/(1 - u'\mu') = -u'$, so that, from equation (A8) and the resonant condition, $\omega' = (\gamma'^2 + 2nb)^{1/2} - \gamma' \leq \omega_n$, since $\gamma' \geq 1$. Boosting with $\beta = \mu$ back to frame K from K', we have $\omega' = \gamma\omega(1 - \beta\mu) = (1 - \mu^2)^{1/2}\omega \leq \omega_n$, which implies that resonant absorption (and hence resonant scattering) is allowed only for $\omega \leq \omega_n/(1 - \mu^2)^{1/2} = \omega_-$.

The scattering profile for $|\mu| = 1$ is given by

$$\phi(\omega, \mu) = \phi_1(\omega, \mu) = c_0 \frac{2}{\omega} f(p_0)(1 + b) , \tag{A11}$$

where

$$p_0 = \frac{\omega^2 - b^2}{2b\omega} \text{ sign } (\mu) . \tag{A12}$$

This profile has a peak at

$$\omega_{pk} = b[(1 + T^2)^{1/2} - T] < b . \tag{A13}$$

When $|\mu| = 1$, the scattering process becomes purely one-dimensional. Since $\sigma_{\rm lab} = (1 - \beta\mu)\sigma_r$, the interaction favors $\beta\mu < 0$, which implies that $\omega < b$ photons (cf. eq. [A12]) have the larger scattering cross section. We therefore expect $\omega_{pk} < b$, as it is. Quite generally, ω_{pk} is a function of temperature, T.

For the profiles with finite natural line width, we let

$$\delta(E_i^r - E_f^r) \rightarrow \frac{\Gamma_n/2\pi}{(E_i^r - E_f^r)^2 + (\Gamma_n/2)^2}$$

in equations (A2) and (A3), where $\Gamma_n \approx n\Gamma_{\rm rad} = 2.6 \times 10^{-3} nB_{12}^2(\text{keV})$ is the radiative width of the nth harmonic. When $|\mu| \neq 1$, $\phi_n(\omega, \mu)$ is given by

$$\phi_n(\omega, \mu) = c_n \int_{-\infty}^{+\infty} dp\, f(p)(1 - \beta\mu)(1 + \mu_r^2)(1 - \mu_r^2)^{n-1} \frac{\Gamma_n/2\pi}{(E_i^r - E_f^r)^2 + (\Gamma_n/2)^2} . \tag{A14}$$

When $|\mu| = 1$, only ϕ_1 is finite and

$$\phi_1(\omega, |\mu| = 1) = 2c_0 \int_{-\infty}^{+\infty} dp\, f(p)(1 - \beta\mu) \frac{\Gamma_n/2\pi}{(E_i^r - E_f^r)^2 + (\Gamma_n/2)^2} . \tag{A15}$$

Cyclotron resonant scattering is forward-backward symmetric. As a result,

$$\phi_n(\omega, \mu) = \phi_n(\omega, -\mu) . \tag{A16}$$

This is evident from equations (A7), (A11), (A14), and (A15).

The integrals in equations (A14) and (A15) are done using Romberg integration. To ensure six digit accuracy or better, we take the integration limits to be ± 1 if $T \leq 0.01$ and ± 10 if $T \leq 0.1$. For use in SAM, we construct two-dimensional tables in (ω, μ) for these profiles. (The zero natural line width profiles are evaluated on-line since they are fully analytic.) We take the grid in μ to be linear between 0 and 1 (exploiting the forward-backward symmetry of the profiles) with an increment of 0.1. For ω, we evaluate the profiles between 0 and 120 keV. Within 1 keV of each resonance, we use a logarithmically spaced grid that samples the profiles densely (30 points) near the resonance. Outside these intervals in between resonances, we use a linear grid with 20 points per interval between resonances.

REFERENCES

Alexander, S. G., & Mészáros, P. 1989, ApJ, 344, L1
Avery, L. W., & House, L. L. 1968, ApJ, 152, 493
Brainerd, J. J. 1992, Nature, 355, 522
Bussard, R. W., & Lamb, F. K. 1982, in AIP Conf. Proc. No. 77, Gamma-Ray Transients and Related Astrophysical Phenomena, ed. R. E. Lingenfelter, H. S. Hudson, & D. M. Worrall (New York: AIP), 189
Clark, G. W., Woo, J. W., Nagase, F., Makishima, K., & Sakao, T. 1990, ApJ, 353, 274
Fenimore, E. E., et al. 1988, ApJ, 335, L71
Gnedin, Yu. N., Pavlov, G. G., & Shibanov, Yu. A. 1978, Soviet Astron. Lett., 4, 117
Harding, A. K., & Preece, R. D. 1989, ApJ, 338, L21
Hueter, G. J. 1984, in AIP Conf. Proc. No. 115, High-Energy Transients in Astrophysics, ed. S. E. Woosley (New York: AIP), 373
Lamb, D. Q., Wang, J. C. L., Loredo, T. J., Wasserman, I., & Fenimore, E. E. 1989, in Proc. 14th Texas Symp. on Relativistic Astrophysics, ed. E. Fenyves (New York: Ann. NY Acad. Sci.), 571, 460
Lamb, D. Q., Wang, J. C. L., & Wasserman, I. 1990, ApJ, 363, 670 (LWW)
Mazets, E. P., et al. 1980, AZh. Pis'ma, 6, 706
Mazets, E. P., Golenetskii, S. V., Aptekar, R. L., Guryan, Yu. A., & Ilyinskii, V. N. 1981, Nature, 290, 378
Meegan, C. A., et al. 1992, Nature, 355, 143
Mészáros, P., & Nagel, W. 1985, ApJ, 298, 147
Mészáros, P., & Ventura, J. 1978, Phys. Rev. Lett., 41, 1544
Mihalas, D. 1978, Stellar Atmospheres (New York: Freeman), Ch. 7
Miller, G. S., Epstein, R. I., Nolta, J. P., & Fenimore, E. E. 1991, Phys. Rev. Lett., 66, 1395
Murakami, T., et al. 1988, Nature, 335, 234
Nagel, W. 1980, ApJ, 236, 904
Nishimura, O., & Ebisuzaki, T. 1992, PASJ, 44, 109
Trümper, J., et al. 1978, ApJ, 219, L105
Wang, J. C. L., Wasserman, I., & Salpeter, E. E. 1988, ApJS, 68, 735
———. 1989a, ApJ, 338, 343
Wang, J. C. L., et al. 1989b, Phys. Rev. Lett., 63, 1550
Wasserman, I. 1992, ApJ, 394, 565
Wasserman, I., & Salpeter, E. 1980, ApJ, 241, 1107
Wheaton, Wm. A., et al. 1979, Nature, 282, 240
Yoshida, A., Murakami, T., Nishimura, J., Kondo, I., & Fenimore, E. E. 1991, PASJ, 43, L69